The 8th European Congress on Computational Methods in Applied Sciences and Engineering
ECCOMAS Congress 2022
5 – 9 June 2022, Oslo, Norway

INVESTIGATION OF PARAMETER-DEPENDENT MATERIAL CHARACTERISTICS OF ADDITIVE MANUFACTURED SPECIMENS FOR DATA-DRIVEN PART OPTIMIZATION

DOMINIC ZETTEL[1,2], PIOTR BREITKOPF[1], PASCAL NICOLAY[2], AND ROLAND WILLMANN[2]

[1] Université de Technologie de Compiègne (UTC)
Laboratoire Roberval
FR3272, CS 60319 60203 Compiègne Cedex, France
email: piotr.breitkopf@utc.fr, www.utc.fr

[2] Carinthia University of Applied Sciences (CUAS)
Additive Manufacturing of Agile Virtual Systems for Product Design and Production Process Design (AMAVIS[2]),
Carinthia Institute for Smart Materials (CiSMAT)
Europastraße 4, 9524 Villach, Austria
email: d.zettel@cuas.at, www.cuas.at

Key words: Direct metal laser sintering, data-driven optimization, multi-physical optimization, tensile strength, microstructure, porosity

Abstract. Direct Metal Laser Sintering (DMLS) is a complex production process including hosts of parameters and a multitude of physical phenomena, which make the simulation and modeling quite challenging. This work investigates the impact of modified printing parameters (e.g., hatch distance, laser power) on correlating material properties (e.g., Young's modulus, temperature gradient) of hardened aluminum specimens. The ultimate goal is to create a data model that enables data-driven and multi-physical optimization of mechanical components fabricated via DMLS.

1 INTRODUCTION

In DMLS, predictive simulation models are not yet available due to the modeling complexity of physical phenomena occurring at different scales and to the lack of accurate material parameters [1]. In addition, the simulation of even simple structures can lead to high computing costs (e.g., model development costs, computing time), which renders the pure simulation approach economically unattractive [2]. The high computing times also result in an increased CO_2 footprint due to energy consumption, cooling systems, etc. [3].

A promising approach for developing predictive simulation models for DMLS parts is to rely on a combination of numerical models and experimental data, as in the spirit of Stainier et al. [4]. In this paper, we propose and describe a method to efficiently determine the required experimental data. Our Design of Experiments (DoE)-based approach included 17 different printing parameter sets, with five cylindrical samples made of "StrengthAl" per parameter set.

The material characteristics (porosity, tensile strength, Young's modulus, and temperature gradient) were investigated using a Reflected Light Microscope (RLM), a Scanning Electron Microscope (SEM), a tensile testing machine, and a self-designed test setup for measuring thermal properties.

The test results, clustered using the K-mean clustering algorithm [5], show a clear correlation between the modified printing parameter settings (laser power, laser speed, hatch distance, and layer thickness) and the material characteristics. It was also recognized that the printing parameters lead to different fracture behavior (brittle and ductile).

This experimental approach constitutes a first step (i.e., determination of material parameters) towards developing predictive simulation models for the multi-physical optimization of DMLS parts, which will not rely on complex process simulation approaches.

2 METHOD AND MATERIAL

The approach regarding the development, fabrication, and testing of aluminum specimens via DMLS consists of three main steps, as schematically shown in Figure 1.

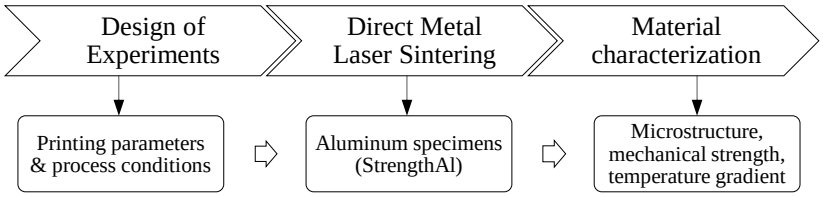

Figure 1: Overall approach regarding the development, fabrication, and testing of aluminum specimens with parameter-dependent material characteristics

A DoE is executed first, in which the material-dependent printing parameter settings, the process conditions of the printing system (e.g., inert gas), and the geometry of the specimens are defined. Then, the specimens are produced. Next, the microstructure, mechanical strength, and temperature gradient of selected specimens are characterized and analyzed. The potential of multi-physical part optimization based on experimental data can be assessed based on the obtained results.

2.1 Design of Experiments

The DoE is based on four factors representing the laser power (P) [W], laser speed (v) [mm/s], hatch distance (h) [mm], and the layer thickness (t) [mm]. These factors are used to determine the overall energy density (E) as follows:

$$E = \frac{P}{v \cdot h \cdot t} \tag{1}$$

In a full factorial design, each parameter can take two different values or "levels" (high and low), resulting in 16 experiments (see Table 1, page 8). We added another experiment (the so-called "center point"), where each parameter takes the average value between the two levels. This "center point" helps to identify non-linear dependencies between factors.

The geometry of the printed specimens is cylindric, with a diameter of 8mm and a height of 103mm. The specimens are attached directly to the build platform without a support structure.

The build platform of the EOS M290 printing system was subdivided into nine grids of equal size, as schematically illustrated in Figure 2. Every printing parameter set of the DoE (1-17) is printed once in every grid ("*a*," "*c*," "*e*," "*g*," "*h*").

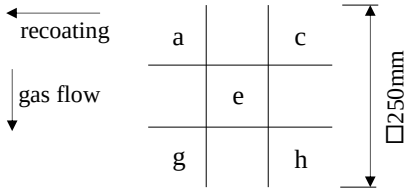

Figure 2: Segmentation of an EOS M290 build platform. Every printing parameter set is printed once in each of the grids "*a*," "*c*," "*e*," "*g*," "*h*" (i.e., 5x17 specimens).

2.2 Direct metal laser sintering

The specimens were fabricated using an EOS M290 printing system with a build volume of 250*250*325mm³ and a 400W Yb-fiber laser with a spot size of 100µm. The applied inert gas is Argon. A ceramic blade is used for powder recoating. The platform temperature is 180°C. The exposure sequence of the specimens is directed against the gas flow to avoid splashes/inclusions within the melt pools. The rotation angle is 67°. The "stripes" exposure pattern is used with a stripe width of 7mm.

The powder material is "StrengthAl" of the company m4p GmbH. StrengthAl is a hardenable high-strength aluminum alloy consisting of Aluminum (main alloying element), Magnesium, Silicon, Scandium, Titanium, Zirconium, Manganese, and Chrome [6].

2.3 Material characterization

Specimen preparation

The specimens were hardened for 6 hours at a temperature of 350°C, followed by slow cooling in the air (precipitation hardening). Then, the specimens were processed using a turning machine to achieve proper test geometries (i.e., in our case, cylinders with a diameter of 7mm and a length of 50mm). The geometry for the tensile tests follows the standard DIN 50125:2016-12 [7] (Form B).

Microstructural characteristics

Three cylinders from grid "*c*" ("*c4*," "*c8*," and "*c10*") were cut in half (side "*A*" and "*B*"), as schematically shown in Figure 3(a). "Side *B"* represents the side of the specimens that was attached to the build platform. Both sides of the specimens were then embedded in Warm Embedding Resin (WER) for subsequent grinding operations. First, the cylinders were roughly ground, up to their longitudinal axis (grinding plane), as shown in Figure 3(b).

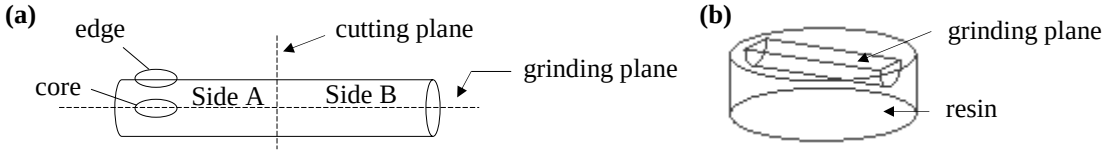

Figure 3: (a): Schematic representation of metallographic specimens including the cutting plane, the grinding plane, and the measurement areas (core and edge) of side "*A*" and "*B.*" **(b):** Sketch of one embedded specimen.

Then, the specimens were ground using Silicon Carbide paper (grain size P1200), a diamond suspension (grain size 3µm), and finally polished using a silicon dioxide suspension (grain size 0.05µm). In a final step, the polished surface was treated with a Keller-Wilcox etchant.

The RLM (Axio Imager.M2m – Zeiss) images of the core area of "side *A*" of the specimens ("*c4*," "*c8*," and "*c10*"), before and after etching, are shown in Figure 4.

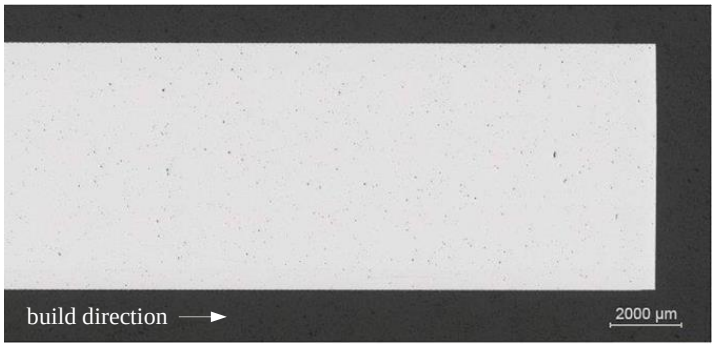

Specimen "*c4*" - "side *A*" (polished, not etched)

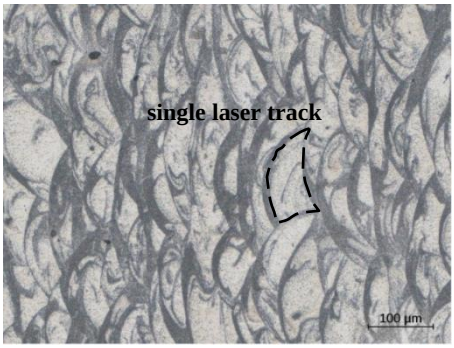

Specimen "*c4*" - "side *A*," core area (polished and etched)

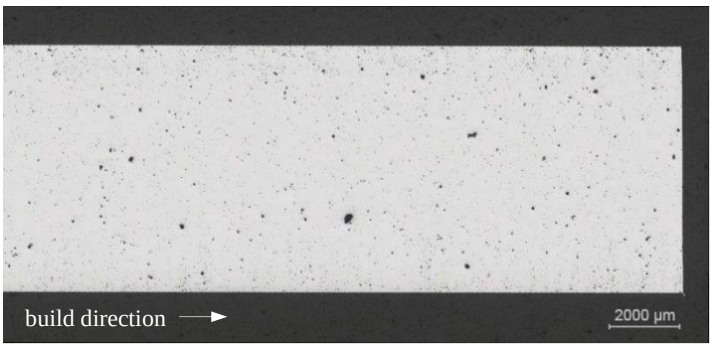

Specimen "*c8*" - "side *A*" (polished, not etched)

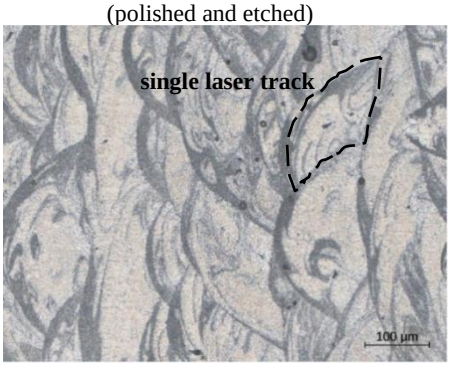

Specimen "*c8*" - "side *A*," core area (polished and etched)

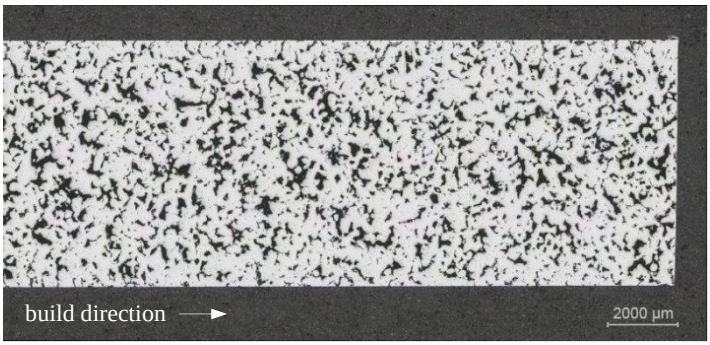

Specimen "*c10*" - "side *A*" (polished, not etched)

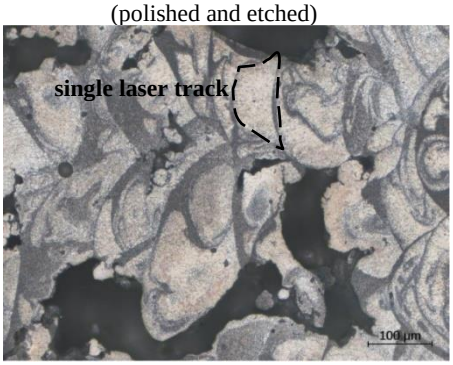

Specimen "*c10* "- "side *A*," core area (polished and etched)

Figure 4: RLM images of aluminum specimens "*c4*," "*c8*," and "*c10*" (polished and etched). **Left column:** RLM images of "side *A*" with polished but not etched surfaces. **Right column:** RLM images of "side *A*" with polished and etched surfaces.

The RLM images in the left column of Figure 4 show the impact of the different printing parameter sets on the specimens' microstructure. There seems to be a correlation between the

applied energy density and the porosity. The lower the energy density, the higher the porosity, as can be seen by comparing the images of specimens "*c4*" (67.34J/mm³) and "*c10*" (14.96J/mm³). The pores appear to be homogeneously distributed within every specimen ("*c4,*" "*c8,*" and "*c10*"). Splashes/inclusions could not be detected in the microstructure.

The RLM images in the right column of Figure 4 show the typical tracks of the laser beam due to the layer-wise manufacturing principle of DMLS.

The porosity (pore size and pore size distribution) of the metallographic specimens was measured using an image processing software (ZEN core – Zeiss). The results of the porosity measurements are shown in Figure 5.

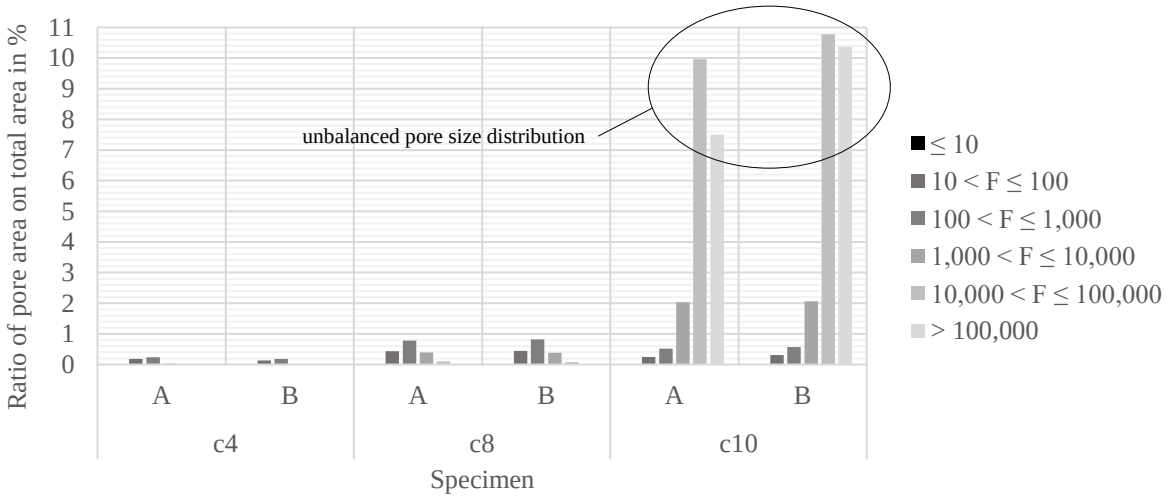

Figure 5: Results of porosity measurements of aluminum specimens fabricated with different printing parameter sets. The diagram shows the impact of the applied energy densities on the pore size and pore size distribution for specimens "*c4,*" "*c8,*" and "*c10.*"

The graph in Figure 5 represents the percentage ratio of pore area to total measurement area of "side *A*" and "side *B*" of the specimens. The pore size and pore size distribution between "side *A*" and "side *B*" of the specimens "*c4*" and "*c8*" seem to be balanced. Whereas the pore size and pore size distribution between "side *A*" and "side *B*" of the specimen "*c10*" is unbalanced. Here, the number of pores with a bigger cross-sectional area than 10,000µm² occur more often on "side *B*" than on "side *A*". This inhomogeneity might be the consequence of variable cooling rates due to the increasing build height of the specimens during the manufacturing process. Here, an increasing build height can lead to heat accumulation in the core area of the specimens, which can affect the microstructure.

Energy Dispersive X-ray Spectroscopy (EDX) was then used to further investigate the metallographic specimens (JSM-IT500 – JEOL). The results show that the alloy elements Aluminum and Magnesium are homogeneously distributed, also in areas around the pores. The remaining alloy elements (Silicon, Scandium, Titanium, Zirconium, Manganese, and Chrome) could not be detected due to the detection limit of the apparatus (0.2% by mass). Figure 6 shows SEM images of "side *A*" of the metallographic specimens "*c4,*" "*c8,*" and "*c10*" before etching.

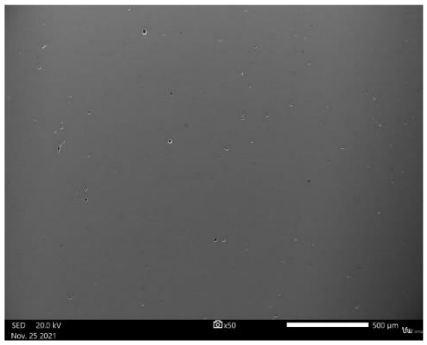

Specimen "*c4*" - "side *A*," core area, polished, not etched (magnification 50x)

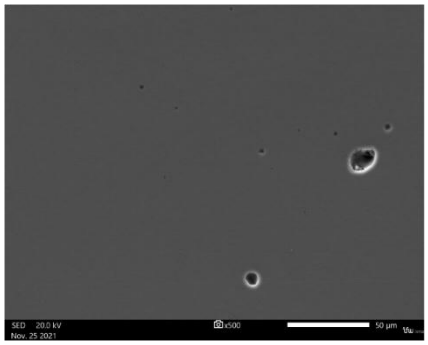

Specimen "*c4*" - "side *A*," core area, polished, not etched (magnification 500x)

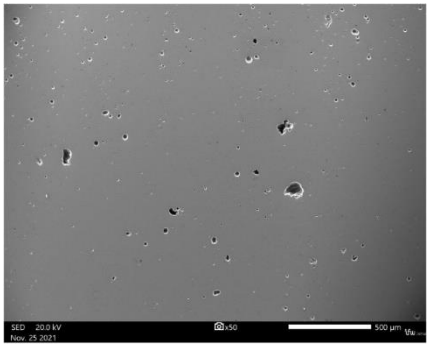

Specimen "*c8*" - "side *A*," core area, polished, not etched (magnification 50x)

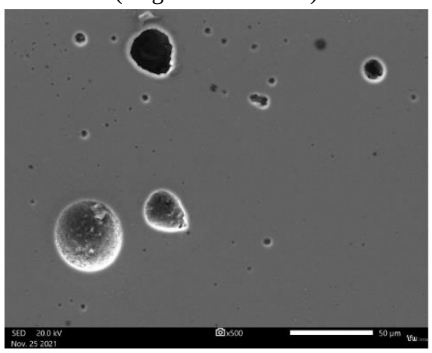

Specimen "*c8*" - "side *A*," core area, polished, not etched (magnification 500x)

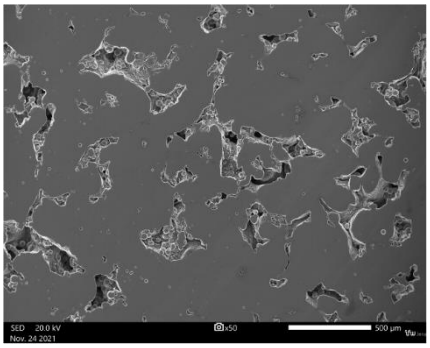

Specimen "*c10*" - "side *A*," core area, polished, not etched (magnification 50x)

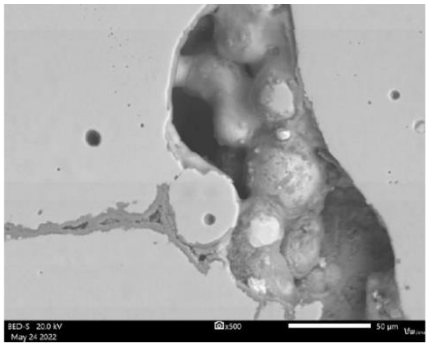

Specimen "*c10*" - "side *A,"* core area, polished, not etched (magnification 500x)

Figure 6: SEM images of aluminum specimens "*c4*," "*c8*," and "*c10*" (polished, not etched). **Left column:** SEM images of "side *A*" with a magnification up to 50x. **Right column:** SEM images of "side *A*" with a magnification up to 500x.

Mechanical characteristics

A tensile testing device (ZwickRoell Z020) was used to investigate the mechanical properties of the specimens from grid "*a*" and grid "*i*." The testing was performed at room temperature (22°C) following the standard ISO 6892-1:2019 [8]. The results of the tensile tests (tensile strength and Young's modulus) are illustrated in Figure 7.

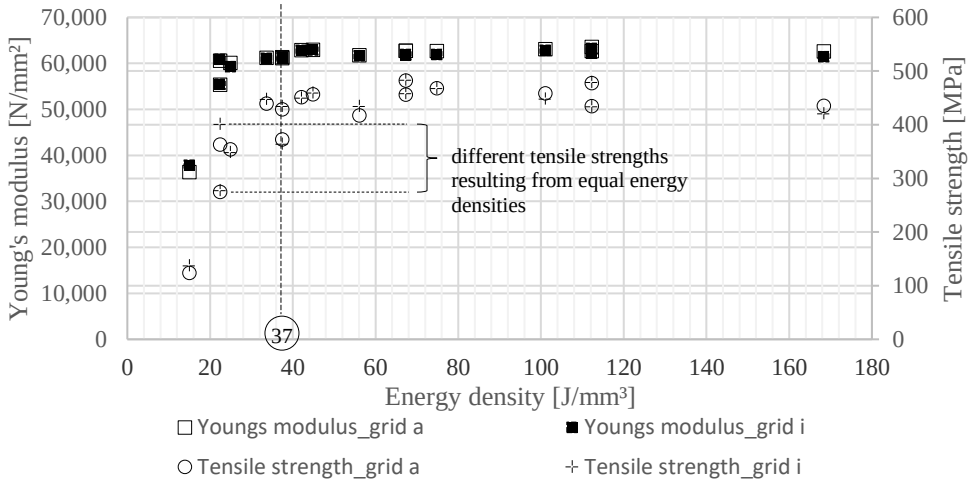

Figure 7: Tensile test results of the 17 different printing parameter sets fabricated in grid "*a*" and grid "*i.*" The diagram shows the tensile strength and the Young's modulus of the specimens.

The data points show good reproducibility between grid "*a*" and grid "*i.*" There is also a clear correlation between the tensile strength and Young's modulus data points. The impact of the different printing parameter sets and their corresponding energy density on the mechanical characteristics are visible. The diagram shows that the tensile strength and Young's modulus rise with increasing energy density. This phenomenon can be observed up to an energy density of about 37J/mm³. Specimens fabricated with energy densities higher than 37J/mm³ do not show significant differences regarding their tensile strength and Young's modulus.

Figure 7 also shows that the energy density does not suffice to classify material characteristics fully. Printing parameter sets with the same energy density (e.g., 22.45J/mm³) show differences in tensile strength and Young's modulus.

The tensile tests also revealed two different microstructures – brittle and ductile. The fractured surfaces and the stress-strain curves of two brittle specimens ("*a13*," "*i13*") and two ductile specimens ("*a1*," "*i1*") are illustrated in Figure 8 and Figure 9.

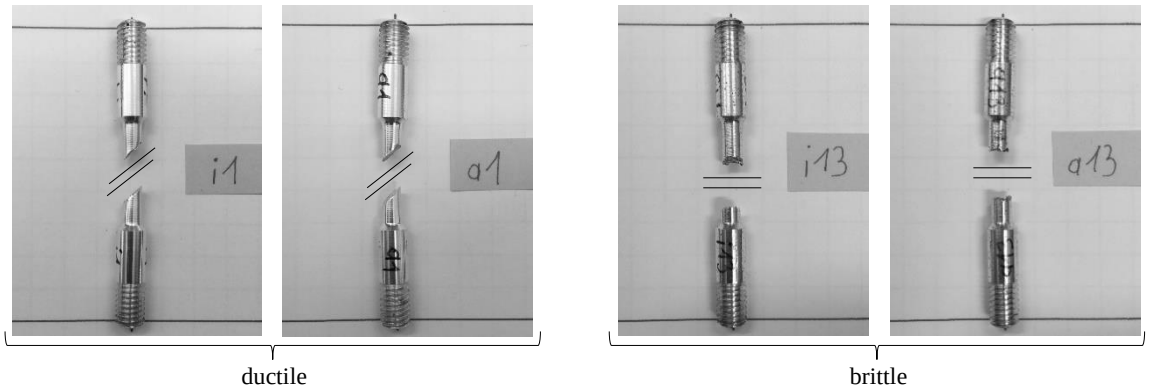

Figure 8: Fragments of DMLS-specimens after tensile testing. **Left:** Typical fractured surfaces of ductile material (shear fracture including necking) of specimens "*i1*" and "*a1*." **Right:** Typical fractured surfaces of brittle material (flat fracture without necking) of specimens "*i13*" and "*a13.*"

Figure 8 shows the typical shear fracture of ductile material (including necking) and the

typical flat fracture of a brittle material (without necking). Figure 9 shows the elastic-plastic deformation of ductile material and the pure elastic deformation of brittle material. The Portevin-Le Chatelier (PLC) [9] effect can also be seen on the left-hand side of Figure 9.

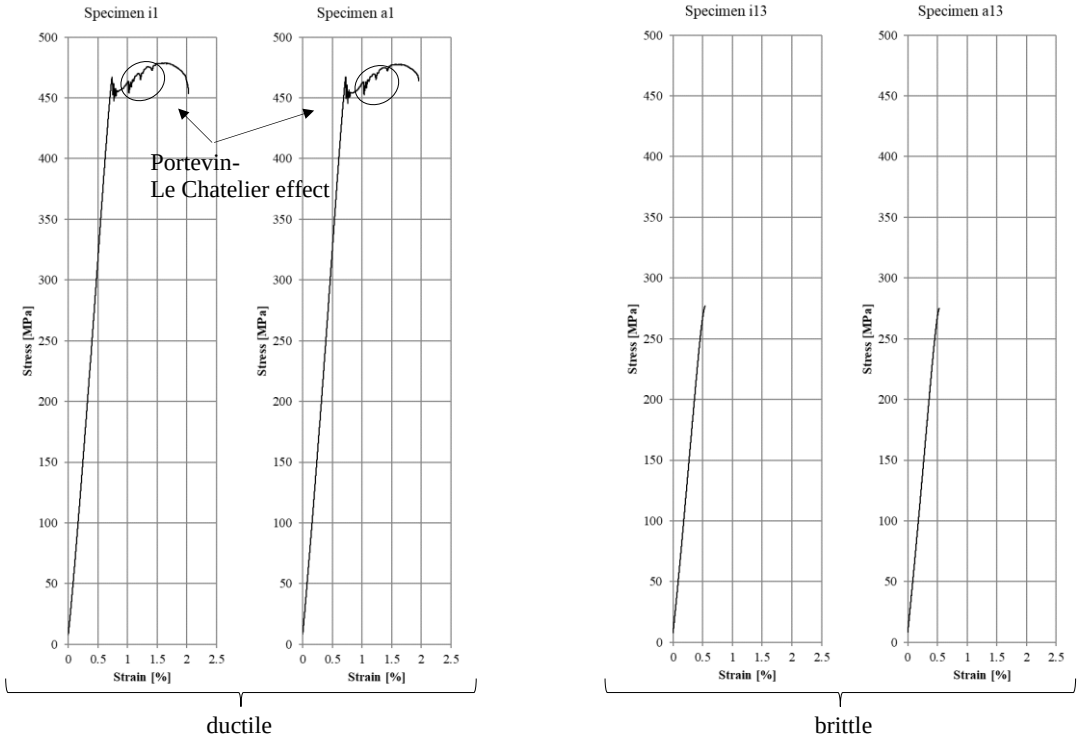

Figure 9: Stress-strain curves of aluminum specimens. **Left:** Typical stress-strain curves of ductile material (elastic-plastic deformation) of specimens "*i1*" and "*a1*." **Right:** Typical stress-strain curves of brittle material (elastic deformation only) of specimens "*i13*" and "*a13.*"

The type of microstructure (brittle/ductile) depends on the applied energy density. The transition boundary between brittle and ductile microstructure is between 37.41J/mm³ and 42.09J/mm³, as shown in Table 1. The only exception to this rule was observed for the parameter set *8* (33.67J/mm³).

Table 1: Full factorial design including printing parameters (*P*, *v*, *h*, *t*) and corresponding energy densities for fabricating aluminum specimens with different material characteristics. The printing parameter sets are sorted according to their energy densities to show the borderline between brittle and ductile structures.

Parameter set	*P* [W]	*v* [mm/s]	*h* [mm]	*t* [mm]	*E* [J/mm³]	
10	200	687.5	0.216	0.09	14.96	
6	300	687.5	0.216	0.09	22.45	
13	200	687.5	0.144	0.09	22.45	
15	200	412.5	0.216	0.09	24.94	brittle
8	300	687.5	0.144	0.09	33.67	
2	200	412.5	0.144	0.09	37.41	
9	300	412.5	0.216	0.09	37.41	
17	250	550	0.18	0.06	42.09	
11	200	687.5	0.216	0.03	44.89	
12	300	412.5	0.144	0.09	56.12	
7	300	687.5	0.216	0.03	67.34	
4	200	687.5	0.144	0.03	67.34	
3	200	412.5	0.216	0.03	74.82	ductile
16	300	687.5	0.144	0.03	101.01	
1	200	412.5	0.144	0.03	112.23	
14	300	412.5	0.216	0.03	112.23	
5	300	412.5	0.144	0.03	168.35	

Thermal characteristics

The temperature gradient of the grid "*g*" and "*e*" specimens was measured using a self-constructed test setup, as schematically illustrated in Figure 10. The test setup consists of a hot plate (50°C) and a cold plate (0°C). Two temperature sensors (PT1000) were bonded on both sides of every specimen. Heat-conducting paste was applied between both plates (hot and cold) and the specimens.

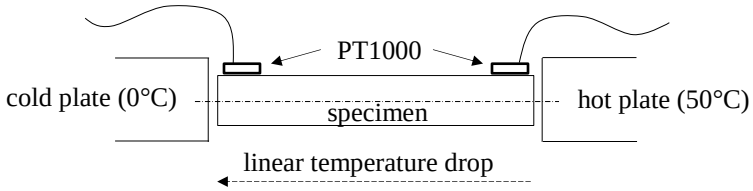

Figure 10: Schematics of self-designed test setup for measuring the temperature gradient of printed specimens.

The results of the temperature gradient measurements of the 17 specimens of grid "*e*" and grid "*g*" are shown in Figure 11.

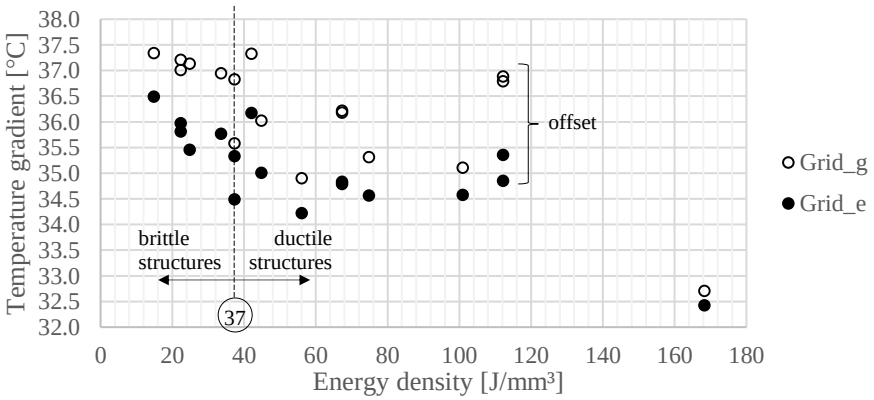

Figure 11: Temperature gradient measurements of aluminum specimens from grids "*e*" and "*g.*" Specimens fabricated with high energy density (ductile structure, e.g., parameter set *5*) show a higher temperature gradient than specimens fabricated with low energy density (brittle structure, e.g., parameter set *10*).

The measurement results of both grids ("*e*" and "*f*") show a clear correlation. The observed offset between the two series of points is due to different room temperatures during testing. Nevertheless, the impact of the different printing parameter sets on the thermal behavior is visible. Specimens with a brittle structure (energy density lower than 37J/mm³) have a higher temperature gradient than specimens with a ductile structure (energy density higher than 37J/mm³). This may result from the specimens' porosity, which is higher in the case of specimens fabricated with low energy density. Pores are full of inert gas acting as a thermal insulator.

Specimens fabricated with different printing parameter settings (*P*, *v*, *h*, *t*) but with the same energy density (e.g., parameter sets *2* and *9*) also show different temperature gradients, which correlates to the tensile test results.

Combined results

The tensile strengths and temperature gradients presented in the previous sections are

juxtaposed concerning the applied energy density, as illustrated in Figure 12.

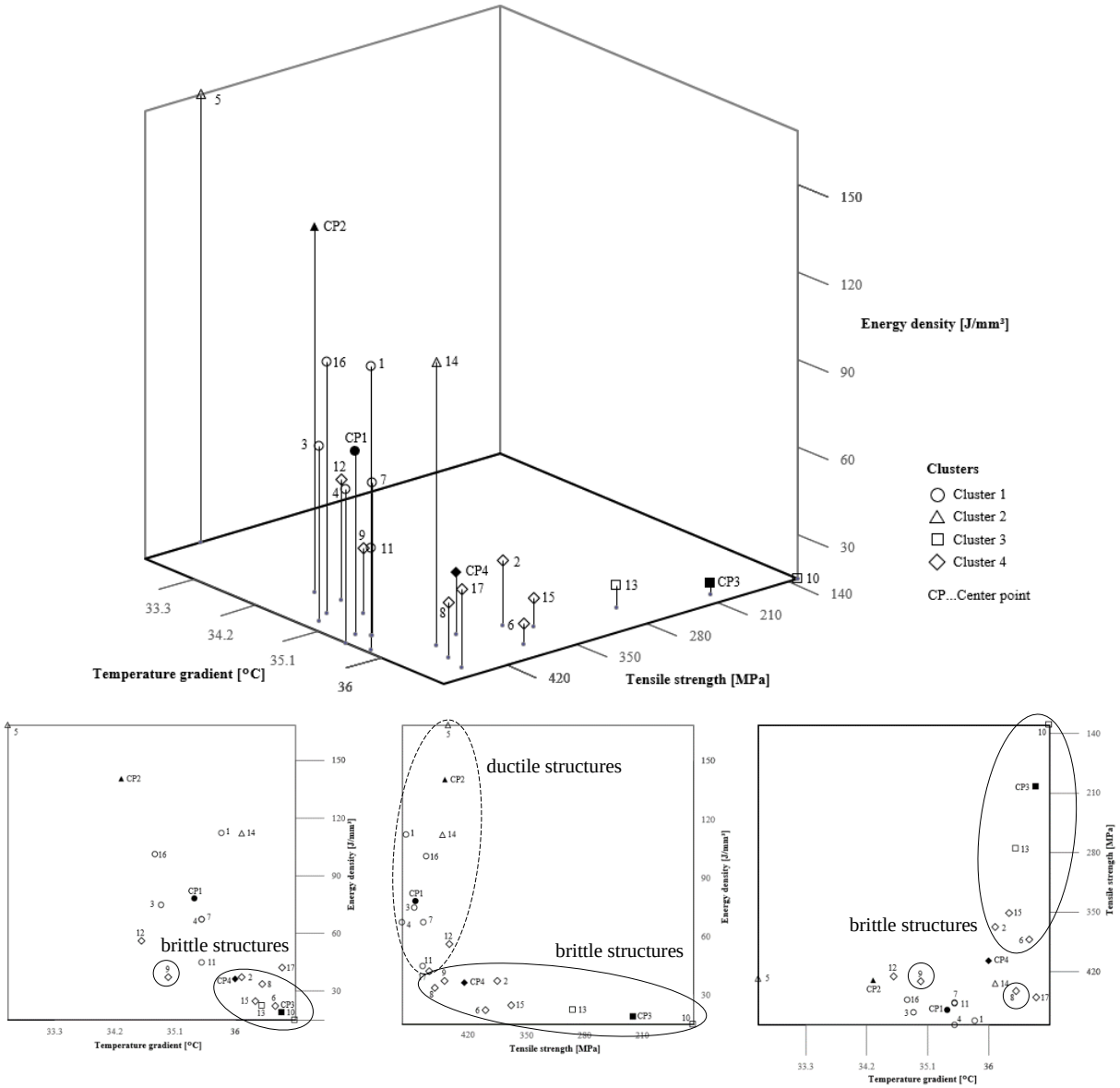

Figure 12: 3D scatter plot including 2D-sections of material data clustered via k-means clustering algorithm. The graph represents the data cloud of temperature gradients and the tensile strengths of the printing parameter sets as a function of their applied energy density. **Bottom left:** Temperature gradient vs. energy density. **Bottom center:** Tensile strength vs. energy density. **Bottom right:** Temperature gradient vs. tensile strength.

The 3D plot of Figure 12 shows the clustered data points (tensile strength and temperature gradient) of the 17 printing parameter sets, including their respective center points (CP). The clustering was performed using the K-means clustering algorithm, which is used to identify groups that have not been explicitly labeled in the data [5] [10] [11]. The number of CPs is arbitrary. We defined four of them. The different views (2D-sections) of the 3D plot enable further interpretation of the results.

The image on the bottom left of Figure 12 shows the energy density's impact on the

specimens' temperature gradient. A compact group of brittle structures (CP1 and CP2) shows a high temperature gradient, which may correlate with the specimens' porosity. The only outlier is the parameter set *9*, which has the thermal behavior of ductile structures. The data points of the ductile structures (CP3 and CP4) show a wider range regarding the temperature gradients.

The image of the bottom center of Figure 12 shows the energy density's impact on the specimens' tensile strength. Here, the different structures (either brittle or ductile) are separated without any outliers. Specimens with brittle structures (CP3 and CP4) show low tensile strength. The correlation between the energy density and the tensile strength of brittle structures appears to be linear. The impact of the energy density on the tensile strength within ductile structures (CP1 and CP2) is quite low. Here, a change in the energy density does not significantly impact the specimens' tensile strength.

The image on the bottom right of Figure 12 shows the correlation between the temperature gradient and the specimens' tensile strength. Brittle structures (CP3 and CP4) seem to have a low tensile strength and a high temperature gradient. Ductile structures (CP1 and CP2) appear to have a high tensile strength and a low temperature gradient. This correlation between thermal and mechanical behavior is non-linear, according to this graph.

3 CONCLUSION

An EOS M290 printing system was used to fabricate 5x17 specimens with different printing parameter sets to investigate their impact on the microstructure and respective material properties (porosity, tensile strength, Young`s modulus, temperature gradient). The modified printing parameters are laser power, laser speed, hatch distance, and layer thickness.

The fractured surfaces and the stress-strain curves of the tensile tests demonstrate that the modified printing parameter sets and their correlating energy densities can result in brittle or ductile microstructures. Brittle specimens have lower tensile strength and Young's modulus than ductile specimens. The boundary between brittle and ductile structures depends on the energy density (37.41J/mm³ and 42.09J/mm³). The tensile tests also revealed that the energy density itself does not suffice to classify the mechanical properties fully. Indeed, specimens with different printing parameter settings (P, v, h, t) but equal energy density present different mechanical characteristics.

The thermal measurements showed that specimens fabricated with a higher energy density (ductile structures) present a lower temperature gradient than specimens fabricated with a lower energy density. The thermal measurements also confirm that the energy density does not suffice to classify the specimens with respect to their thermal properties.

The results of the mechanical and thermal measurements were superimposed and clustered using the K-means clustering algorithm. The results show no direct correlation between the brittle or ductile behavior and the other material properties. The correlation between mechanical and thermal properties also appears to be non-linear.

In future work, damping factors, surface roughness, and thermal conductivity will be measured to complement the preliminary results published in this paper and help interpret the observed data.

ACKNOWLEDGEMENT

This work was conducted in the frame of research cooperation between the research group

Additive Manufacturing in Agile Virtual Systems for Product Design and Production Process Design (AMAVIS^2), the Carinthia Institute for Smart Materials (CiSMAT), and the Laboratoire ROBERVAL of the Université de Technologie de Compiègne (UTC). AMAVIS^2 and CiSMAT belong to the Carinthia University of Applied Sciences (CUAS). The work was fully funded by AMAVIS^2.

REFERENCES

[1] J. Zhang, Y. Zhang, W. H. Lee, L. Wu, H.-H. Choi and Y.-G. Jung, "A multi-scale multi-physics modeling framework of laser powder bed fusion additive manufacturing process," *Metal Powder, Vol. 73, No. 3, ISSN: 0026-0657,* pp. 151-157, June 2018.

[2] The Minerals, Metals & Materials Society (TMS), "Modeling Across Scales: A Roadmapping Study for Connecting Materials Models and Simulations Across Length and Time Scales," The Minerals, Metals & Materials Society (TMS), ISBN 9780692376065, Warrendale, PA 15086, 2015.

[3] B. Saha, "Green Computing," *International Journal of Computer Trends and Technology (IJCTT), volume 14 number 2, ISSN 2231-2803*, pp. 46-50, August 2014.

[4] L. Stainier, A. Leygue and M. Ortiz, "Model-free data-driven methods in mechanics: Material data identification and solvers," *Computational Mechanics, Springer, HAL Id: hal-02159717,* p. 381–393, June 2019.

[5] J. Wu, Advances in K-means Clustering: A Data Mining Thinking - 1st edition, Berlin, Germany: Springer Science & Business Media, ISBN 9783642298073, 2012.

[6] m4p material solutions GmbH, "www.metals4printing.com," 2022. [Online]. Available: https://www.metals4printing.com/wp-content/uploads/datasheets/eng/Al-Base/m4p_Datasheet_StrengthAl_EN.pdf. [Accessed 02 May 2022].

[7] DIN Deutsches Institut für Normung, "www.beuth.de," 2022. [Online]. Available: https://www.beuth.de/de/norm/din-50125/262241217. [Accessed 2 May 2022].

[8] Österreichisches Normungsinstitut (ON), "www.beuth.de," 2022. [Online]. Available: https://www.beuth.de/de/norm/din-en-iso-6892-1/317931281. [Accessed 2 May 2022].

[9] E. A. Chechulina, D. S. Gribov, F. S. Popov, R. M. Gerasimov and P. V. Trusov, "Three-level dislocation-oriented model: An application to the description of the Portevin-Le Chatelier effect," *Proceedings of the International Conference "Physical Mesomechanics. Materials with Multilevel Hierarchical Structure and Intelligent Manufacturing Technology", Volume 2509, Issue 1, 10.1063/5.0084498,* 22 April 2022.

[10] R. Scitovski, K. Sabo, F. Martínez-Álvarez and S. Ungar, Cluster Analysis and Applications - 1st edition, Cham, Switzerland: Springer Nature, ISBN 9783030745523, 2021.

[11] C. C. Aggarwal and C. K. Reddy, Data Clustering: Algorithms and Applications - 1st edition, Florida, United States of America: CRC Press, ISBN 9781315360416, 2018.